Nanoscale

PAPER

View Article Online
View Journal | View Issue

Cite this: *Nanoscale*, 2025, **17**, 28006

Toward scalable manufacturing of doped silicon nanopillars for thermoelectrics *via* metal-assisted chemical etching

Federico Giulio, * Luca Calciati,† Filippo Andreotti, Andrea Brevi and Dario Narducci

Received 16th August 2025,
Accepted 21st November 2025

DOI: 10.1039/d5nr03474d

rsc.li/nanoscale

Metal-Assisted Chemical Etching (MACE) using Ag as the catalyst lets prepare vertically aligned crystalline silicon nanopillars (SiNPs), a highly promising system for thermoelectric applications, with high aspect ratios in a wide doping range. MACE may be implemented either by using Ag both as the catalyst and the oxidant (so-called one-pot MACE) or by using another chemical (typically H_2O_2) as the oxidant (two-pot MACE). This study investigates how the localized etching rate depends upon Si doping in both MACE implementations, accounting for the concurrent non-catalyzed etching. The latter, which shortens SiNPs, is found to become more significant in p-type Si at higher doping levels due to the narrower space-charge regions at the bare Si-solution interface. We demonstrated that in both one- and two-pot MACE the etching rate is controlled by the band bending at silicon–silver interface. In p-type silicon, it decreases with doping due to faster hole diffusion, while the Schottky barrier at the interface hinders hole injection in n-type silicon at any doping level. Overall, we highlight that MACE may be effectively implemented in its one-pot version, facilitating MACE scale-up toward SiNP large-scale manufacturing.

1. Introduction

In recent years silicon nanopillars have attracted considerable interest due to their unique and versatile properties. Their high aspect ratio, quasi-one dimensionality, inducing quantum confinement, and tunable electrical, thermal, and optical properties[1] make them suitable in several technologies. In photovoltaics, Si nanopillars (SiNPs) are used as absorbing layers[2] and as anti-reflective coatings.[3] They also found applications in sensing[4] and bio-sensing,[5] in photoelectrochemistry,[6] as electrodes in Li-ion batteries[7] and in energy storage.[8] Furthermore, SiNPs display a large thermoelectric figure of merit[9] compared to bulk single-crystalline Si (with a figure of merit of 0.01) due to the enhanced phonon scattering when their diameter is smaller than the phonon mean free path.[10–13] Thermoelectric modules based on SiNPs have been fabricated and characterized,[14,15] achieving figures of merit up to 0.24 at 700 K with a thermoelectric module where SiNP arrays were grown on both sides of a silicon wafer.[16]

Several techniques have been exploited to produce SiNPs, both bottom-up and top-down,[17] including Vapor–Liquid Solid,[18] Molecular Beam Epitaxy[19] and cryogenic Reactive Ion Etching.[20] However, they all require ultra-high-vacuum conditions, which severely limit their scalability. Additionally, the growth rate is low, also often resulting in low density SiNPs.[21]

Metal-Assisted Chemical Etching (MACE) provides a remarkable alternative, as it enables SiNP to be obtained at room temperature and ambient pressure with high densities, very high aspect ratios and excellent crystalline quality.[22] Moreover, MACE allows full control of SiNP orientation and, in principle, lets obtain SiNPs of arbitrary length. The technique is based on the local silicon oxidation catalyzed by metallic nanoparticles, which can be generated either *in situ* from a metallic salt or deposited *via* physical methods.[23] More specifically, when the metal acts both as the catalyst and the oxidant (*e.g.* using Ag/Ag^+) the procedure is referred to as one-pot MACE. Instead, when the metal is used only as the catalyst while the oxidation is carried out by a different chemical (*e.g.* H_2O_2), it is known as two-pot MACE. blueOne-pot MACE is a simpler technque, as it does not require multiple solutions, thereby minimizing processing time and cost. In contrast, the two-pot MACE process follows a sequential approach, in which the catalyst nanoparticles are deposited on the Si surface (by either physical or chemical methods) prior to the etching step, at the cost of greater complexity. However, two-pot MACE

Department of Materials Science, University of Milano-Bicocca, Via Roberto Cozzi 55, 20125 Milano, Italy. E-mail: federico.giulio@unimib.it

†Present address: Department of Environmental Sciences, Informatics and Statistics, Ca' Foscari University of Venice, Via Torino 155, 30170, Venezia Mestre, Italy.

offers greater versatility, as the pattern of metal nanoparticles can be tailored to produce different nanostructures such as nanosheets or nanorods.[23] Both in one- and two-pot MACE, the etch rate depends on several parameters, including temperature,[24] illumination,[25] concentration of the oxidizing agent and of HF,[9,26] metal catalyst and the shape of its nanoparticles.[27,28] Moreover, the etch rate exhibits a stronger dependence on both silicon dopant type and concentration and, since MACE is a technique amenable to be brought to industrial production grade, it is essential to achieve full control over the etch rate for different types of silicon. The aim of this paper is to investigate how Si doping level and type impact MACE etch rate where Ag is used as the catalyst, for both one- and two-pot processes. Numerous studies in the literature have investigated the influence of silicon dopant type and level on the etch rate in MACE. Lai *et al.*[29] studied two-pot MACE using gold as a catalyst and H_2O_2 as the oxidizing agent. They reported that the etch rate decreases with increasing dopant concentration for p-type silicon, while, for n-type silicon, it remains nearly constant with increasing phosphorus concentration. This behavior was attributed to the formation of Schottky barriers. Similarly, Ohlin *et al.*[30] demonstrated that under the same MACE conditions (gold and H_2O_2), n-type silicon etches faster than p-type silicon at the same doping level. Backes *et al.*[31] explored two-pot MACE using silver as a catalyst. Their results show a decrease in the etch rate with increasing doping level for p-type silicon, confirming their previous results,[32] while for n-type silicon, the etch rate remains constant at low and medium doping levels. They explain these trends with the presence of Schottky barrier in n-type silicon that trapped the carrier at the interface, while in p-type silicon the etch rate is ruled by the carrier diffusion away from the metal semiconductor interface. In contrast to the above findings, Bagal *et al.*[33] observed an increase of the etch rate with doping level for both n-type and p-type silicon when using silver and H_2O_2, suggesting a different doping-dependence trend under their conditions. Further supporting this observation, Li *et al.*[34] reported a decrease in the etch rate for n-type silicon with increasing doping concentration using silver as the catalyst. Interestingly, they noted that this trend reversed when accounting for the effects of lateral etching because of the dissolution and re-nucleation of metallic silver. To the best of our knowledge, instead, no detailed study has reported the etch rate of one-pot MACE as a function of silicon doping level and type. We will show that the etch rate dramatically changes moving from n- to p-type silicon, in striking contrast with what is observed for non-catalyzed etching. Charge injection and accumulation/depletion at the relevant interface between metal, silicon, and the electrolytic solution are shown to rule the etch rate.

2. Experimental

Single-crystalline CZ Si (100) wafers used in this investigation are listed in Table 1. For each type and doping, eight samples were prepared, four with one-pot MACE and four with two-pot MACE, with reaction times of 96, 192, 330 and 370 minutes in both processes.

Table 1 Silicon substrates used to evaluate the etching rate as a function of the doping level. The resistivity of the silicon samples, and consequently their carrier density, was determined using the four-probe method[35]

Type	Dopant	Resistivity (Ω cm)	Doping level (cm^{-3})	Thickness (μm)
p^-	B	11.6	1.3×10^{15}	660
p	B	0.7	2.5×10^{16}	450
p^+	B	0.02	4.0×10^{18}	525
n^-	P	6.1	7.4×10^{14}	280
n	P	0.08	1.1×10^{17}	380
n^+	P	0.003	2.0×10^{19}	500

The samples were prepared with the following procedure: Silicon chips (1.5 × 0.5 cm^2) were cleaved from [100]-oriented p- and n-type silicon substrates. The samples were cleaned using ammonium-peroxide solution (1 : 1 : 5 NH_3 (29% vol.) : H_2O_2 (33% vol.) : H_2O)[36] at 65 °C for 15 minutes and then rinsed in deionized (DI) water, removing all organic contaminants. Samples were then immediately soaked in the MACE solution. For one-pot MACE, $AgNO_3$ (16 mM) and HF (5 M) were used. Instead, for two-pot reaction, the samples were firstly immersed in a solution containing $AgNO_3$ (5 mM) and HF (5 M) for 1 minute and then rinsed in DI water. Afterward, the silver-coated samples were immersed in the etching solution (H_2O_2, 0.4 M + HF, 8 M). For both processes the temperature was kept constant at 20 °C with a thermostatic bath. For all silicon samples, in both one- and two-pot MACE, etching occurred on both sides of the wafer, resulting in a double NP forest. At the end of the MACE processes the samples were immediately soaked in DI water to stop the reaction and then in a solution containing HNO_3 (32% vol.) for 15 minutes to remove silver dendrites and nanoparticles, then rinsed in DI and finally dried using a nitrogen flux. SiNP length and morphology were evaluated by Scanning Electron Microscopy (SEM). SEM analyses were performed with a ThermoFisher Phenom G6 SEM, equipped with a thermionic emission source. This instrument achieves a resolution <6 nm at 15 kV using a Everhart–Thornley type detector for secondary electrons.

3. Results and discussion

At any doping level and for both one- and two-pot processes, dense and crystalline SiNPs were obtained, with a diameter that ranges from 100 to 150 nm, namely lower than Si phonon mean free path (300 nm (ref. 37)) (Fig. 1 and S1), and therefore, expected to display reduced thermal conductivity. In all samples, in-plane SEM analyses show SiNP tip agglomeration (Fig. S2) due to capillarity forces arising during the drying process after MACE termination.[38–40]

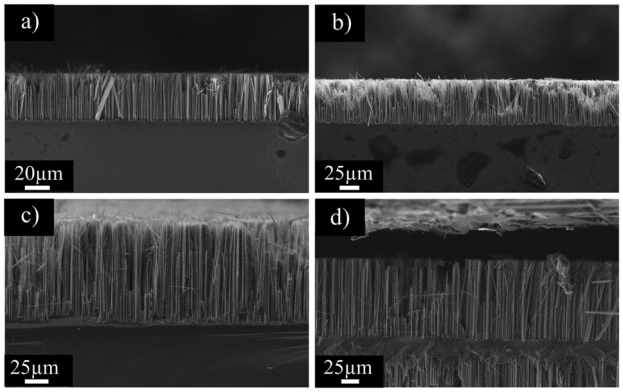

Fig. 1 Cross section SEM images of n^- SiNPs obtained after 2-pot MACE reaction at differing etching time: 96 min (a), 192 min (b) 330 min (c) and 370 min (c).

To obtain a proper estimate of the MACE rate, one should consider that, in addition to MACE, etching also occurs on the bare Si surface, including SiNP tips. We will refer to this non-localized etching as *overetching*. Therefore, in what follows we first measured the dependence of overetching rate and its variation upon doping level and type; then, after measuring the apparent MACE rate, we corrected it accounting for the tip removal by overetching.

3.1. Overetching

The following results have been obtained performing both one-pot ($[AgNO_3]$ = 16 mM and [HF] = 5 M) and two-pot ($[H_2O_2]$ = 0.4 M and [HF] = 8 M) MACE.

By measuring the total thickness of the obtained samples, which includes the SiNP forests and the silicon layer beneath them, it is evident that the etched samples have a reduced thickness compared to the pristine silicon wafer (Fig. 2). This thickness loss was observed for both MACE processes and for both doping types.

Thickness loss is evaluated as the difference between the pristine wafer thickness and the thickness of the samples, after MACE processes, for different reaction times. By plotting the thickness loss as a function of the reaction time, the overetching rate can be determined from the slope of the resulting line. The overetching rate as a function of the doping level for both n- and p-type silicon, and for both MACE processes, is reported in Fig. 3.

Overetching is more relevant in two-pot MACE than in one-pot and, moreover, the higher the doping level the higher the overetching rate for both p- and n-type substrates.

Two effects concur to such difference. From SEM analyses (Fig. 4) one observes the occurrence of etching pits on the tips and on the sidewalls of the wires. The formation of these additional localized etching sites arises from the reoxidation of metallic silver, with Ag^+ subsequently undergoing reduction back to metallic silver. The redeposited Ag preferentially accumulates in energetically favorable regions and defects-rich sites such as the tips or walls of the nanopillars.[41]

Such *silver shuttling* is more pronounced in two-pot MACE. Indeed, in this case, silver nanoparticles located at the bottom of the bores can be oxidized by the hydrogen peroxide, which has a more positive redox potential than the Ag^+/Ag couple (0.80 V and 1.78 V *vs.* SHE, respectively), and re-nucleate on the sidewall, reducing the effective length of the SiNPs.[42]

Silver shuttling is detectable also in one-pot MACE but the presence of the dendritic structures, which completely overfill the bores, partially hinders it, leading to a smaller thickness loss. Moreover in one-pot MACE the species that can re-oxidize silver is water, a weaker oxidant compare to hydrogen peroxide. Furthermore, in both one- and two-pot MACE, the presence of defects is higher in more heavily doped substrates, further promoting the formation of lateral etching sites,[43] in accordance with measured overetching rates (Fig. 3).

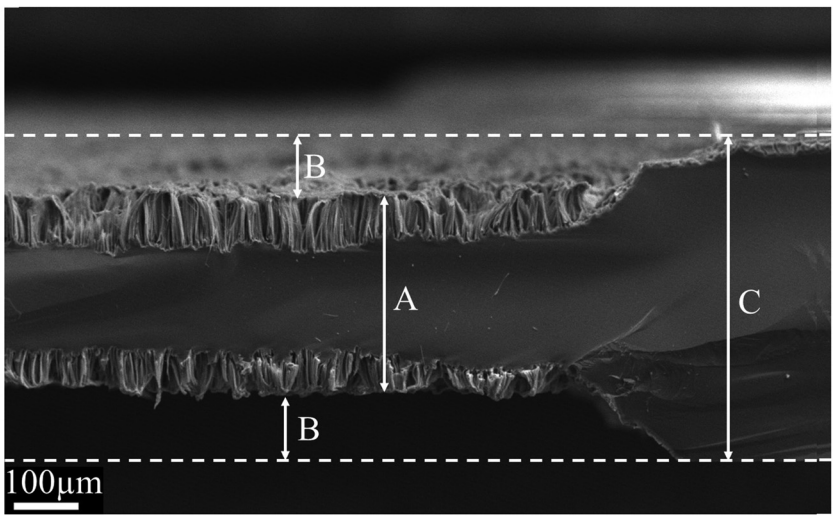

Fig. 2 Reduced thickness on p^+ SiNPs obtained after one-pot MACE reaction (480 min). C is the pristine silicon wafer thickness, A is the overall thickness (SiNPs plus silicon membrane) after MACE and B is the material loss.

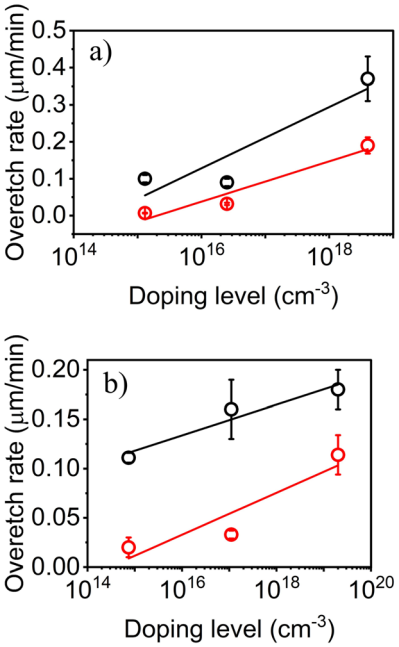

Fig. 3 Overetching rates *vs.* doping level for (a) p-type samples obtained with one-pot MACE (red) and 2-pot MACE (black). In (b) the rates for n-type samples obtained with one-pot MACE (red) and 2-pot MACE (black).

The second process that contributes to the thickness loss is the *non-localized* etching, basically the direct hole exchange between solution and silicon that occurs everywhere on the bare silicon surface. Non-localized etching always takes place and competes with localized etching, being eventually dominant,[11,44] and occurs both in one- and two-pot MACE.

To better understand non-localized etching and its relation with silicon doping level, the interface between silicon and the oxidant solution is analyzed (Fig. 5 and Fig. S4).

In all cases, once contact is established and equilibrium conditions are reached, Fermi level of the semiconductor aligns with the redox potential of the oxidizing couple.[45,46] In one-pot MACE the interface is ruled by the Ag^+/Ag potential (Fig. 5) while in two-pot is determined by the H_2O_2/H_2O redox potential (Fig. S4). Since both the potential of Ag^+/Ag and H_2O_2/H_2O are more negative than the Fermi energies (Tables S1 and S2), bands always bend upward. Potential drop occurs almost entirely at the semiconductor side. In all cases, a potential barrier is formed at the silicon/solution interface. Thus, the injection of holes, from the solution into the valence band, and, consequently, their diffusion into the silicon bulk is hindered, leading to hole accumulation in the space-charge region near the silicon surface. The thickness of this space-charge region depends on the doping level and on the oxidizing strength of the redox couple. Specifically, the region narrows as the doping level increases. This is clearly noticeable in both Fig. 5 and S4. Indeed, in one-pot MACE the space-charge region in p^--type is approximately 800 nm wide, while in p^+-type is just 20 nm. A similar trend is observed for n^--type silicon (≈1250 nm *versus* ≈12 nm in n^+-type) as shown in Fig. 5. Same behaviour can be observed in two-pot MACE for both silicon types (Fig. S4). Since the etching rate is correlated with the hole density near the silicon surface, a narrower space-charge region leads to a more pronounced overetching. This competes with localized etching, resulting in a more significant loss of thickness. Consequently, non-localized etching

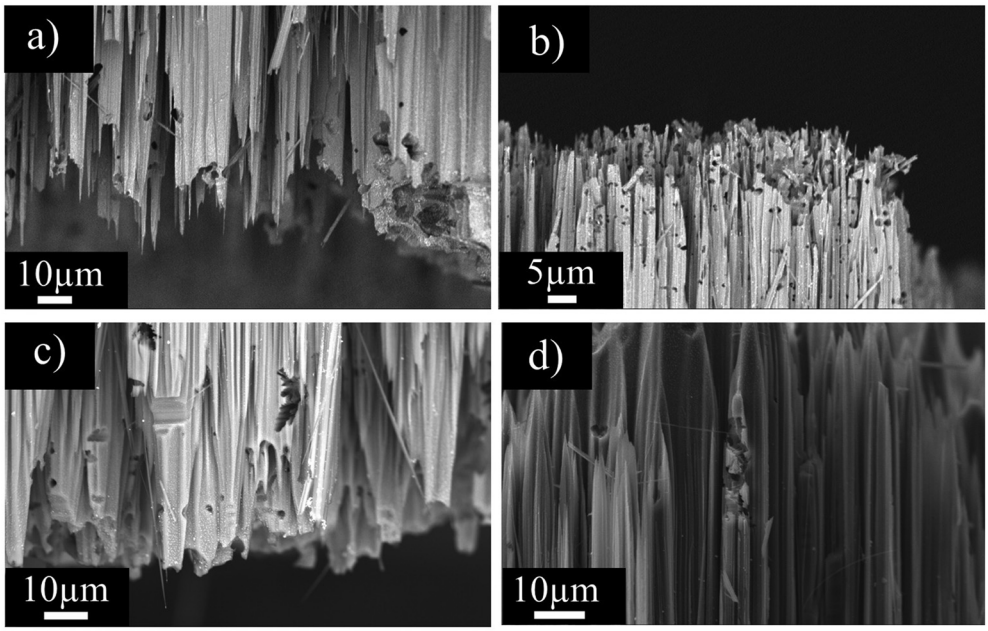

Fig. 4 Cross section SEM micrographs showing the effect of silver shuttling on the SiNP tips and sidewall. (a) and (b) on p-type SiNPs obtained with two-pot MACE and (c) and (d) on n-type SiNPs after one-pot MACE.

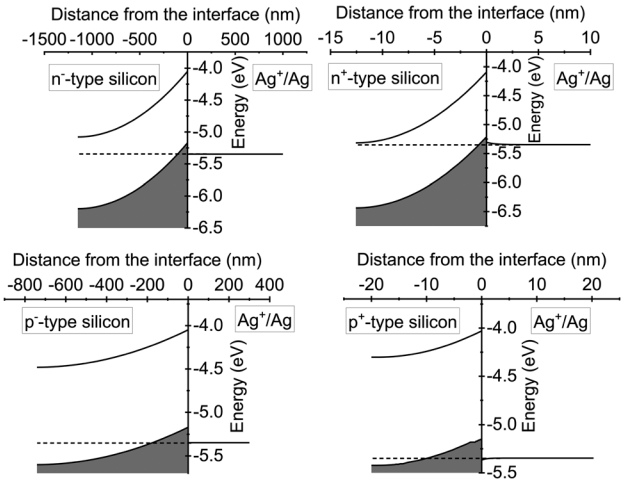

Fig. 5 Silicon band bending at equilibrium and at zero bias upon contact with Ag^+/Ag electrolyte solution, for p^-, p^+, n^-, and n^+ samples. The energy is referred to the vacuum level. Note that the space charge width decreases moving from low to high doped silicon, both for p- and n-type substrates.

is more prominent at higher doping levels, because the accumulation region is only a few tens of nanometers thick. In contrast, in lightly doped silicon, the accumulation region is wider, allowing diffusion of holes from the surface into the silicon bulk. This makes non-localized etching less effective, favouring the formation of SiNPs.

3.2. Localized etch rate

As it is known, in one-pot MACE silver nanoparticles are generated *in situ* from a silver salt, like $AgNO_3$, according to the electroless cathodic reduction:

$$Ag_{(aq)}^{+} \rightarrow Ag_{(s)} + h^{+} \quad E^{\circ} = +0.79\ \text{V}\ vs.\ \text{NHE} \tag{1}$$

In this way metallic silver particles are deposited onto silicon surface and holes are injected into silicon valence band. Over time, these particles evolve in complex dendritic structures reaching a height of several microns. The dendrimers completely overfill the etching bores.[24] In the meantime, oxidation of silicon takes place. Two competing anodic reactions concurrently occur:[11,26] the first reaction is called 4-electron process and is the reaction ruling silicon electropolishing.[47] Silicon is directly oxidized to Si^{4+}:

$$\begin{aligned} &Si_{(s)} + 4h^{+} + 6H_2O_{(aq)} \rightarrow SiO_{2(s)} + 4H_3O^{+} \\ &E^{\circ} = -0.84\,\text{V}\,vs.\,\text{NHE} \end{aligned} \tag{2}$$

and subsequently SiO_2 is etched away by HF:

$$SiO_{2(s)} + 6HF_{(aq)} \rightarrow {SiF_{6(aq)}}^{2-} + 3H_3O^{+} \tag{3}$$

The alternative oxidation path is known as 2-electron process. In this case, silicon is initially oxidized to Si^{2+}:

$$\begin{aligned} &Si_{(s)} + 2h^{+} + 4HF_{(aq)} + 4H_2O_{(aq)} \rightarrow {SiF_{4(aq)}}^{2-} + 4H_3O^{+} \\ &E^{\circ} = -1.20\,\text{V}\,vs.\,\text{NHE} \end{aligned} \tag{4}$$

Then Si^{2+} is oxidized to Si^{4+} with the concurrent reduction of two hydronium ions to molecular hydrogen:

$${SiF_{4(aq)}}^{2-} + 2HF_{(aq)} \rightarrow {SiF_{6(aq)}}^{2-} + H_{2(g)} \tag{5}$$

The 4-electron reaction is dominant for low-doped silicon substrates. In this case the oxide dissolution is the slow reaction step, leading to a smooth and regularly etched silicon surface or, when localized, to the formation of single-crystalline SiNPs. *Vice versa*, on highly doped silicon, 2-electron process prevails, the oxide elimination being the fast reaction step that leads to the formation of a porous silicon layer or, when localized, to (partially) porous SiNPs.[24]

Two-pot MACE occurs instead in two different steps.[48] First of all, the deposition of catalytic metallic nanoparticles takes place. This step could be performed either *via* chemical reduction of metallic cations in solution or by using physical methods like evaporation or sputtering. The second step is the silicon oxidation in a solution containing both the oxidant and HF. Typically, hydrogen peroxide (H_2O_2) is used as oxidant. Hydrogen peroxide injects holes into silicon according to the reaction:[26]

$$\begin{aligned} &H_2O_{2(aq)} + 2H^{+} \rightarrow 2H_2O_{(aq)} + 2h^{+} \\ &E^{\circ} = +1.35\,\text{V}\,vs.\,\text{NHE} \end{aligned} \tag{6}$$

Oxidation of silicon and the oxide etching follow either the 4-electron or the 2-electron path, as in one-pot MACE.

Since the chemistry of one- and two-pot MACE is the same, one expects that etch rates should be comparable in the two processes. By plotting the SiNP lengths as a function of reaction time, the apparent localized etch rate for each doping level is obtained (Fig. 6), along with the effective etch rates. The latter was computed by taking into account the NP thickness loss due to overetching (Fig. 7). Essentially, the effective

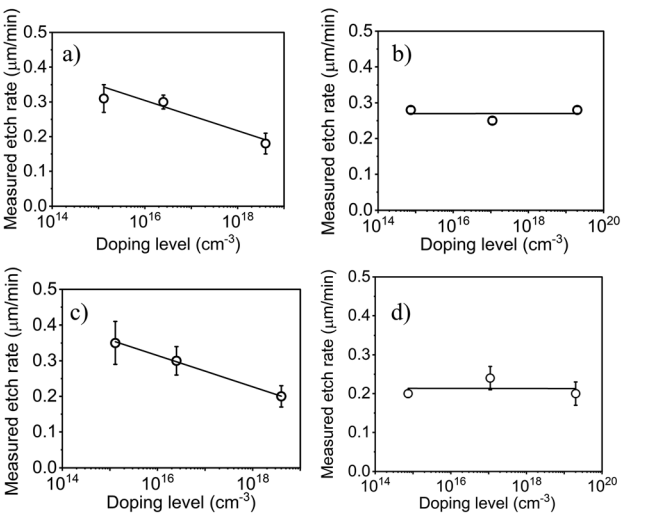

Fig. 6 Etch rates as function of the doping level. (a) One-pot MACE etch rate for p-type silicon and (b) for n-type silicon, while in (c) and (d) two-pot MACE etch rate for p- and n-type silicon respectively.

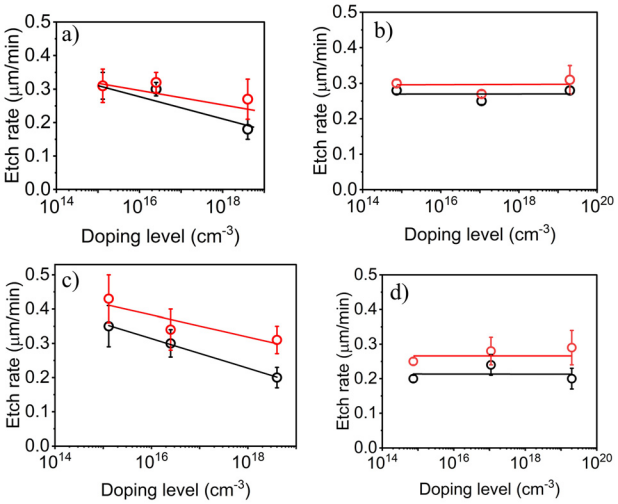

Fig. 7 Comparison between the apparent etch rate (black) and the effective one (red), computed considering the overetching, as function of the doping level for (a) one-pot MACE p-type, (b) one-pot MACE n-type, (c) two-pot MACE p-type and (d) two-pot MACE n-type silicon substrates.

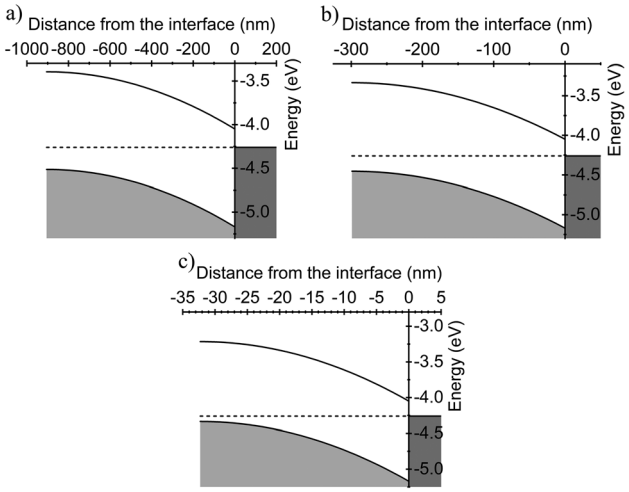

Fig. 8 Band bending induced by the intimate contact between polycrystalline silver and p-type silicon at different doping level: p^- (a), p (b) and p^+ SiNPs (c). The energy is referred to the vacuum level.

etch rate is the etch rate in the absence of overetching. As expected the effective etch rates are higher. The largest increase in the effective etch rate is noticeable for the highly doped samples. Nonetheless, in n-type samples, for both the one- and two-pot processes, the effective etch rate remains almost constant, confirming no dependence on the doping level. Instead, for p-type samples, the higher the doping level the lower the etch rate for both MACE processes.

Etch rate for p^- and p samples is similar, while at higher doping level it suddenly decreases for both one- and two-pot MACE. In contrast, in n-type samples the etch rate remains almost constant with varying doping levels. Thus, no qualitative difference in localized etch rate is observed between one-pot and two-pot MACE. Moreover, the SEM images in Fig. 1 and S1 show no noticeable morphological differences between the NPs obtained by one- and two-pot MACE.

To understand the different etching behaviour between n- and p-type silicon one should consider the interface between silicon and the catalytic metal (Fig. 8 and Fig. S3). When silver enters in intimate contact with silicon, Fermi level aligns with the metal work function, leading to a band bending in the semiconductor side – and to a potential drop thereof. The extent of band bending depends on the Fermi levels of the semiconductor (set by its doping level and type) and on the metal work function (4.26 eV for polycristalline silver[24]) (Fig. 8). This is manifestly the same in both one and two-pot MACE since bending depends solely on the relative position of the Fermi level and the silver work function, which are not affected by the oxidant species. Thus, the localized etch rate is ruled by the silicon/silver interface.

For all doping level the presence of metallic silver pins the Fermi energy and the band folds downward. Thus, no potential barrier hindering hole injection into the valence band and their diffusion toward silicon bulk is present. According to Lai *et al.*,[29] who observed similar results in two-pot MACE using gold as a catalyst, in p-type silicon the absence of a potential barrier means that the concentration of holes is ruled by their drift velocity away from the interface. The drift velocity, in turn, depends both on the hole mobility and on the electric field strength at the interface. As doping increases, mobility decreases while the electric field increases, since at higher doping level the space-charge region narrows, dropping from ≈900 nm in p^- samples to ≈300 nm in p samples and to just ≈33 nm in p^+ Si. Therefore, p^- and p samples exhibit similar drift velocities and, as a result, comparable etch rates. Instead, in p^+ silicon, the electric field strength becomes dominant, compensating for the reduced mobility. Thus, holes move away from the interface, causing a lower etch rate.

In the case of n-type silicon (Fig. S3), while for lightly doped samples there is a slight downward band bending, in samples with higher doping levels, the bands bend upwards, displaying the formation of a potential barrier at the silver/silicon interface. The barrier, in the case of n and n^+ Si, opposes to the injection of holes into silicon valence band confining the holes near the interface. Consequently, the etch rate is similar regardless of the doping level.

It is worth mentioning that when the silicon/silver system is immersed in the solution, another interface is also formed, namely the one between silver and the electrolyte solution. The potential drop that occurs at the interface can be computed using the classical metal/solution interface and can be described with the standard electrical double layer model.[49] However, the calculated potential drop at the Ag/electrolyte interface is significantly smaller than that at the Si/Ag interface and therefore does not affect the silicon band bending and does not play a relevant role in the MACE mechanism. This is in agreement with literature reports.[45,46] Further details on the band bending calculations and interface modeling are reported in the SI.

4. Summary and conclusion

In this study we investigated the etch rate as a function of silicon doping type and concentration, also accounting for the overetching phenomenon. The latter consistently reduces the effective SiNP length. The impact of overetching becomes more pronounced with increasing doping level, independently of dopant type. This behavior was attributed to the simultaneous enhancement of silver shuttling and non-localized etching under high doping conditions. Indeed, in highly doped silicon the increased density of defects facilitates silver shuttling by promoting the dissolution and re-nucleation of metallic silver on SiNP tips and sidewalls. Moreover, silver shuttling is generally more pronounced in two-pot MACE process compared to one-pot. This is due to the higher oxidative potential of H_2O_2 (1.77 V *vs.* SHE) which can re-oxidize metallic silver more easily than O_2 and H_2O (1.23 V *vs.* SHE) in one-pot MACE. Additionally, the space-charge region at the silicon/electrolytic solution interface becomes significantly narrower in highly doped substrates, increasing the hole density near the silicon surface and favoring non-localized etching. As a result, the overall SiNP length loss becomes more substantial. This trend highlights the critical need to account for overetching when precise control over SiNP length is required, particularly in highly doped silicon substrates.

When analyzing the effective etch rate, which includes losses due to overetching, no substantial difference is observed between one-pot and two-pot MACE. This indicates that the etching is primarily governed by the silicon/silver interface through the doping level and type of the semiconductor. In p-type silicon, where silver does not form a Schottky barrier, the etch rate decreases with doping concentration due to the fast hole diffusion away from the interface. In highly doped p-type samples the reduction in hole mobility is compensated by the increased electric field strength at the interface, resulting from the narrower space charge region compared to low-doped samples. This stronger field accelerates hole drift away from the interface, preventing effective participation in the etching reaction and thus reducing the etch rate. In contrast, for n-type silicon, the presence of a Schottky barrier at the interface hinders hole injection, resulting in an etch rate largely independent of doping level. These findings are in agreement with Lai *et al.*[29] and Backes *et al.*[31,32] who observed similar results in two-pot using both gold and silver as catalyst. Notably, our study extends this understanding to include one-pot MACE, showing that even with different oxidant environments, the same doping-dependent trends hold on, confirming the key role of the silicon/silver interface in governing the etch rate.

In conclusion, this study provides deeper insight into the fundamental mechanisms governing MACE for different doped silicon type. By demonstrating that the etch rate is ruled by interfacial processes at the silicon/silver junction, rather than by the type of MACE process, we simplify the choice between one-pot and two-pot strategies for various applications. This flexibility is particularly valuable for scalable manufacturing of SiNPs. Additionally, the role of overetching is highlighted as a critical factor affecting final SiNP length, especially in highly doped silicon.

Author contributions

FG: writing – original draft, review & editing, investigation, formal analysis, conceptualization, methodology. LC: investigation, formal analysis. FA: investigation. AB: investigation. DN: writing – review & editing, conceptualization, methodology, project administration, funding acquisition, supervision.

Conflicts of interest

There are no conflicts to declare.

Data availability

Data for this article, including the etch rate showed in Fig. 3, 6 and 7, are available at Bicocca Open Archive Research Data at https://board.unimib.it/datasets/bk82wc727y/1, https://doi.org/10.17632/bk82wc727y.1.

Supplementary information (SI) is available. See DOI: https://doi.org/10.1039/d5nr03474d.

Acknowledgements

F. G. acknowledges the support received by the Ministry of University and Research in the frame of the PON Program 'Research & Innovation' 2014–2020, Axis IV, Action IV.5, Grant DOT 13C6492. All authors acknowledge funding by the European Union – Next Generation EU, Mission 4 Component 1 CUP H53D23003770006.

References

1 T. Arjmand, M. Legallais, T. T. T. Nguyen, P. Serre, M. Vallejo-Perez, F. Morisot, B. Salem and C. Ternon, Functional Devices from Bottom-Up Silicon Nanowires: A Review, *Nanomaterials*, 2022, **12**, 1043.
2 D. Das and K. Sarkar, Growth Mechanism and Opto-Structural Characterization of Vertically Oriented Si Nanowires: Implications for Heterojunction Solar Cells, *ACS Appl. Energy Mater.*, 2024, **7**, 6649–6666.
3 C. Yao, Y. Liu, J. Niu, C. Lu, H. Li and C. Xie, Micro/nano-hybrid hierarchical structure of black silicon decorated with gold nanoparticles for ultralow broadband reflectivity, *Appl. Surf. Sci.*, 2024, **655**, 159641.
4 V. Kashyap, H. Pawar, C. Kumar, N. Chaudhary and K. Saxena, Analysis of synthesized doped vertical silicon nanowire arrays for effective sensing of nitrogen dioxide: As gas sensors, *Front. Mater.*, 2022, **9**, 1022317.

5 W. Zhao, J. Hu, J. Liu, X. Li, S. Sun, X. Luan, Y. Zhao, S. Wei, M. Li, Q. Zhang and C. Huang, Si nanowire Bio-FET for electrical and label-free detection of cancer cell-derived exosomes, *Microsyst. Nanoeng.*, 2022, **8**, 57.
6 T. S. Teitsworth, D. J. Hill, S. R. Litvin, E. T. Ritchie, J.-S. Park, J. P. Custer, A. D. Taggart, S. R. Bottum, S. E. Morley, S. Kim, J. R. McBride, J. M. Atkin and J. F. Cahoon, Water splitting with silicon p–i–n superlattices suspended in solution, *Nature*, 2023, **614**, 270–274.
7 S. A. Ahad, T. Kennedy and H. Geaney, Si Nanowires: From Model System to Practical Li-Ion Anode Material and Beyond, *ACS Energy Lett.*, 2024, **9**, 1548–1561.
8 A. A. Leonardi, A. Arrigo, M. J. Lo Faro, F. Nastasi and A. Irrera, 2D Fractal Arrays of Ultrathin Silicon Nanowires as Cost-Effective and High-Performance Substrate for Supercapacitors, *Adv. Energy Sustainability Res.*, 2024, **5**, 2400080.
9 E. Dimaggio, D. Narducci and G. Pennelli, Fabrication of Silicon Nanowire Forests for Thermoelectric Applications by Metal-Assisted Chemical Etching, *J. Mater. Eng. Perform.*, 2018, **27**, 6279–6285.
10 A. I. Boukai, Y. Bunimovich, J. Tahir-Kheli, J.-K. Yu, W. A. Goddard III and J. R. Heath, Silicon nanowires as efficient thermoelectric materials, *Nature*, 2008, **451**, 168–171.
11 A. I. Hochbaum, D. Gargas, Y. J. Hwang and P. Yang, Single Crystalline Mesoporous Silicon Nanowires, *Nano Lett.*, 2009, **9**, 3550–3554.
12 X. Zianni, Thermal conductivity engineering in width-modulated silicon nanowires and thermoelectric efficiency enhancement, *J. Phys. D: Appl. Phys.*, 2018, **51**, 114003.
13 L. Yang, D. Huh, R. Ning, V. Rapp, Y. Zeng, Y. Liu, S. Ju, Y. Tao, Y. Jiang, J. Beak, J. Leem, S. Kaur, H. Lee, X. Zheng and R. S. Prasher, High thermoelectric figure of merit of porous Si nanowires from 300 to 700K, *Nat. Commun.*, 2021, **12**, 3926.
14 S. Lee, K. Kim, D.-H. Kang, M. Meyyappan and C.-K. Baek, Vertical Silicon Nanowire Thermoelectric Modules with Enhanced Thermoelectric Properties, *Nano Lett.*, 2019, **19**, 747–755.
15 S. Elyamny, E. Dimaggio, S. Magagna, D. Narducci and G. Pennelli, High Power Thermoelectric Generator Based on Vertical Silicon Nanowires, *Nano Lett.*, 2020, **20**, 4748–4753.
16 R. Ning, Y. Zeng, V. Rapp, B. Zhang, L. Yang, R. Prasher and X. Zheng, Thermoelectric performance of high aspect ratio double-sided silicon nanowire arrays, *J. Appl. Phys.*, 2024, **135**, 095001.
17 V. Schmidt, J. V. Wittemann and U. Gösele, Growth, Thermodynamics, and Electrical Properties of Silicon Nanowires, *Chem. Rev.*, 2010, **110**, 361–388.
18 Y. Zhu, F. Xu, Q. Qin, W. Y. Fung and W. Lu, Mechanical Properties of Vapor-Liquid-Solid Synthesized Silicon Nanowires, *Nano Lett.*, 2009, **9**, 3934–3939.
19 P. Werner, N. D. Zakharov, G. Gerth, L. Schubert and U. Gösele, On the formation of Si nanowires by molecular beam epitaxy, *Int. J. Mater. Res.*, 2006, **97**, 1008–1015.
20 J. Xu, *et al.*, Deep-reactive ion etching of silicon nanowire arrays at cryogenic temperatures, *Appl. Phys. Rev.*, 2024, **11**, 021411.
21 K.-K. Lew and J. M. Redwing, Growth characteristics of silicon nanowires synthesized by vapor–liquid–solid growth in nanoporous alumina templates, *J. Cryst. Growth*, 2003, **254**, 14–22.
22 Z. Huang, N. Geyer, P. Werner, J. de Boor and U. Gösele, Metal-ssisted Chemical Etching of Silicon: A Review: In memory of Prof. Ulrich Gösele, *Adv. Mater.*, 2010, **23**, 285–308.
23 S. Surdo and G. Barillaro, Voltage- and Metal-assisted Chemical Etching of Micro and Nano Structures in Silicon: A Comprehensive Review, *Small*, 2024, **20**, 2400499.
24 S. Magagna, D. Narducci, C. Alfonso, E. Dimaggio, G. Pennelli and A. Charaï, On the mechanism ruling the morphology of silicon nanowires obtained by one-pot metal-assisted chemical etching, *Nanotechnology*, 2020, **31**, 404002.
25 Z. Dong, W. Rong, Y. Zhang and X. Deng, Light-Assisted MACE Method for the Control of Silicon Nanowire Morphology, *IOP Conf. Ser.: Mater. Sci. Eng.*, 2018, **394**, 032102.
26 C. Chartier, S. Bastide and C. Lévy-Clément, Metal-assisted chemical etching of silicon in HF-H_2O_2, *Electrochim. Acta*, 2008, **53**, 5509–5516.
27 F. Toor, J. B. Miller, L. M. Davidson, L. Nichols, W. Duan, M. P. Jura, J. Yim, J. Forziati and M. R. Black, Nanostructured silicon via metal assisted catalyzed etch (MACE): chemistry fundamentals and pattern engineering, *Nanotechnology*, 2016, **27**, 412003.
28 F. J. Wendisch, M. Rey, N. Vogel and G. R. Bourret, Large-Scale Synthesis of Highly Uniform Silicon Nanowire Arrays Using Metal-Assisted Chemical Etching, *Chem. Mater.*, 2020, **32**, 9425–9434.
29 R. A. Lai, T. M. Hymel, V. K. Narasimhan and Y. Cui, Schottky Barrier Catalysis Mechanism in Metal-Assisted Chemical Etching of Silicon, *ACS Appl. Mater. Interfaces*, 2016, **8**, 8875–8879.
30 H. Ohlin, T. Frisk, I. Sychugov and U. Vogt, Comparing metal assisted chemical etching of N and P-type silicon nanostructures, *Micro Nano Eng.*, 2023, **19**, 100178.
31 A. Backes, A. Bittner, M. Leitgeb and U. Schmid, Influence of metallic catalyst and doping level on the metal assisted chemical etching of silicon, *Scr. Mater.*, 2016, **114**, 27–30.
32 A. Backes and U. Schmid, Impact of doping level on the metal assisted chemical etching of p-type silicon, *Sens. Actuators, B*, 2014, **193**, 883–887.
33 I. V. Bagal, M. A. Johar, M. A. Hassan, A. Waseem and S.-W. Ryu, Facile morphology control of high aspect ratio patterned Si nanowires by metal-assisted chemical etching, *J. Mater. Sci.: Mater. Electron.*, 2018, **29**, 18167–18177.
34 H. Li, S. Kato and T. Soga, Etching rate of silicon nanowires with highly doped silicon during metal-assisted chemical etching, *Mater. Res. Express*, 2022, **9**, 115007.

35 G. Masetti, M. Severi and S. Solmi, Modeling of carrier mobility against carrier concentration in arsenic-, phosphorus-, and boron-doped silicon, *IEEE Trans. Electron Devices*, 1983, **30**, 764–769.
36 R. Hull, *Properties of Crystalline Silicon*, INSPEC, Institution of Electrical Engineers, 1999, p. 1042.
37 Y. S. Ju and K. E. Goodson, Phonon scattering in silicon films with thickness of order 100 nm, *Appl. Phys. Lett.*, 1999, **74**, 3005–3007.
38 A. S. Togonal, L. He, P. Roca i Cabarrocas and E. Rusli, Effect of Wettability on the Agglomeration of Silicon Nanowire Arrays Fabricated by Metal-Assisted Chemical Etching, *Langmuir*, 2014, **30**, 10290–10298.
39 S. Maurya, R. C. Muduli and P. Kale, Physical Forces Responsible for Agglomeration of Silicon Nanowires Arrays Synthesized by Metal-Assisted Chemical Etching, *Russ. J. Phys. Chem. A*, 2023, **97**, 1990–2000.
40 F. Giulio, L. Puccio, S. Magagna, A. Perego, A. Mazzacua and D. Narducci, Self-Sustained Quasi-1D Silicon Nanostructures for Thermoelectric Applications, *ACS Appl. Electron. Mater.*, 2023, **6**, 2917–2924.
41 Y. Qu, H. Zhou and X. Duan, Porous silicon nanowires, *Nanoscale*, 2011, **3**, 4060.
42 X. Zhong, Y. Qu, Y.-C. Lin, L. Liao and X. Duan, Unveiling the Formation Pathway of Single Crystalline Porous Silicon Nanowires, *ACS Appl. Mater. Interfaces*, 2011, **3**, 261–270.
43 Z. R. Smith, R. L. Smith and S. D. Collins, Mechanism of nanowire formation in metal assisted chemical etching, *Electrochim. Acta*, 2013, **92**, 139–147.
44 S. Li, W. Ma, Y. Zhou, X. Chen, Y. Xiao, M. Ma, W. Zhu and F. Wei, Fabrication of porous silicon nanowires by MACE method in $HF/H_2O_2/AgNO_3$ system at room temperature, *Nanoscale Res. Lett.*, 2014, **9**, 196.
45 X. G. Zhang, *Electrochemistry of Silicon and Its Oxide*, Springer, 2001, p. 522.
46 G. Oskam, J. G. Long, A. Natarajan and P. C. Searson, Electrochemical deposition of metals onto silicon, *J. Phys. D: Appl. Phys.*, 1998, **31**, 1927–1949.
47 X. G. Zhang, S. D. Collins and R. L. Smith, Porous Silicon Formation and Electropolishing of Silicon by Anodic Polarization in HF Solution, *J. Electrochem. Soc.*, 1989, **136**, 1561–1565.
48 A. A. Leonardi, M. J. L. Faro and A. Irrera, Silicon Nanowires Synthesis by Metal-Assisted Chemical Etching: A Review, *Nanomaterials*, 2021, **11**, 383.
49 A. J. Bard and L. R. Faulkner, *Electrochemical Methods: Fundamentals and Applications*, Wiley, 2001, p. 833.